

Snow Equi-Temperature Metamorphism Described by a Phase-Field Model Applicable on Micro-Tomographic Images: Prediction of Microstructural and Transport Properties

L. Bouvet, N. Calonne, F. Flin, C. Geindreau

▶ **To cite this version:**

L. Bouvet, N. Calonne, F. Flin, C. Geindreau. Snow Equi-Temperature Metamorphism Described by a Phase-Field Model Applicable on Micro-Tomographic Images: Prediction of Microstructural and Transport Properties. Journal of Advances in Modeling Earth Systems, 2022, 14, 10.1029/2022MS002998 . insu-03863738

HAL Id: insu-03863738
https://insu.hal.science/insu-03863738

Submitted on 21 Nov 2022

HAL is a multi-disciplinary open access archive for the deposit and dissemination of scientific research documents, whether they are published or not. The documents may come from teaching and research institutions in France or abroad, or from public or private research centers.

L'archive ouverte pluridisciplinaire **HAL**, est destinée au dépôt et à la diffusion de documents scientifiques de niveau recherche, publiés ou non, émanant des établissements d'enseignement et de recherche français ou étrangers, des laboratoires publics ou privés.



Distributed under a Creative Commons Attribution - NonCommercial - ShareAlike 4.0 International License

Check for updates

JAMES | Journal of Advances in Modeling Earth Systems

RESEARCH ARTICLE
10.1029/2022MS002998

Snow Equi-Temperature Metamorphism Described by a Phase-Field Model Applicable on Micro-Tomographic Images: Prediction of Microstructural and Transport Properties

L. Bouvet[1,2], N. Calonne[1], F. Flin[1], and C. Geindreau[2]

[1]Univ. Grenoble Alpes, Université de Toulouse, Météo-France, CNRS, CNRM, Centre d'Études de la Neige, Grenoble, France, [2]Université Grenoble Alpes, Grenoble INP, 3SR, CNRS, Grenoble, France

Key Points:

- A phase-field model of mean curvature flow is applied on the process of sublimation-deposition, describing equi-temperature metamorphism
- The model is calibrated through the condensation coefficient parameter by fitting experimental and simulated data at −2°C
- Equi-temperature metamorphism is predicted on different snow microstructures; morphological and transport property changes are analyzed

Supporting Information:

Supporting Information may be found in the online version of this article.

Correspondence to:

L. Bouvet,
lisa.bouvet@univ-grenoble-alpes.fr

Citation:

Bouvet, L., Calonne, N., Flin, F., & Geindreau, C. (2022). Snow equi-temperature metamorphism described by a phase-field model applicable on micro-tomographic images: Prediction of microstructural and transport properties. *Journal of Advances in Modeling Earth Systems*, *14*, e2022MS002998. https://doi.org/10.1029/2022MS002998

Received 24 JAN 2022
Accepted 23 JUN 2022

© 2022 The Authors. Journal of Advances in Modeling Earth Systems published by Wiley Periodicals LLC on behalf of American Geophysical Union. This is an open access article under the terms of the Creative Commons Attribution-NonCommercial-NoDerivs License, which permits use and distribution in any medium, provided the original work is properly cited, the use is non-commercial and no modifications or adaptations are made.

Abstract Representing snow equi-temperature metamorphism (ETM) is key to model the evolution and properties of the snow cover. Recently, a phase-field model describing mean curvature flow evolution on 3D microstructures was proposed (Bretin et al., 2019, https://doi.org/10.1051/m2an/2018075). In the present work, this model is used to simulate snow ETM at the pore scale, considering the only process of moving interfaces by sublimation-deposition driven by curvatures. We take 3D micro-tomographic images of snow as input in the model and obtain a time series of simulated microstructures as output. Relating the numerical time, as defined in the model, to the real physical time involves the condensation coefficient α, a poorly constrained parameter in literature. A calibration was performed by fitting simulations to experimental data through the evolution of specific surface area (SSA) of snow under ETM at −2°C. A value of the condensation coefficient was obtained: $(9.8 \pm 0.7) \times 10^{-4}$ and was used in all the following simulations. We then show that the calibrated model enables to well reproduce an independent time series of ETM at −2°C in terms of SSA, covariance length, and mean curvature distribution. Finally, the calibrated model was used to investigate the effect of ETM on microstructure and effective transport properties (thermal conductivity, vapor diffusion, and permeability) for four different samples. As an interesting preliminary result, simulations show an enhancement of the structural anisotropy of snow in the case of initially anisotropic microstructures, such as depth hoar. Results highlight the potential of such microscale models for the development of snow property predictions for large-scale snowpack models.

Plain Language Summary Snow on the ground is a skeleton of ice in air evolving continuously under different environmental constraints. When the temperature gradient within the snowpack is weak, the snow grains tend to gradually become smoother and rounder. This so-called equi-temperature metamorphism (ETM) is one of the main mechanisms of snow evolution and its correct representation is crucial for snow modeling. Here, we use a mean curvature flow model, describing the smoothing of 3D microstructures, to simulate snow ETM. 3D micro-tomographic images of snow samples are used as input; the output is a time series of 3D images showing ETM evolution. Describing ETM classically relies on the condensation coefficient α, a poorly constrained parameter, which drives the intensity of the evolution. We estimate this parameter for ETM at −2°C by fitting simulations to experimental data. Based on comparisons with an independent data set, we show that the model enables to well reproduce ETM at −2°C when no significant densification occurs. Finally, we use the model to investigate the effect of ETM on microstructure and effective transport properties of snow for four different samples. Overall, this work presents promising tools for snow metamorphism study and the development of predictive means for large-scale snow models.

1. Introduction

Dry snow on the ground is a complex material made of an ice skeleton in an air matrix that undergoes continuous transformations. Especially, snow evolves through processes of mass redistribution due to thermodynamic mechanisms called snow metamorphism. Different types of snow metamorphism take place depending on the temperature and humidity conditions as well as on the snow microstructure itself (see, e.g., Calonne, Flin, et al., 2014; Colbeck, 1997; Flin et al., 2004; Hammonds et al., 2015). Considering metamorphism is key as it impacts snowpack physical properties, including mechanical properties involved in avalanche processes or thermophysical properties that drive the surface energy budget of the snowpack (Lehning et al., 2002; Vionnet et al., 2012).

19422466, 2022, 9, Downloaded from https://agupubs.onlinelibrary.wiley.com/doi/10.1029/2022MS002998 by Cochrane France, Wiley Online Library on [21/11/2022]. See the Terms and Conditions (https://onlinelibrary.wiley.com/terms-and-conditions) on Wiley Online Library for rules of use; OA articles are governed by the applicable Creative Commons License

19422466, 2022, 9, Downloaded from https://agupubs.onlinelibrary.wiley.com/doi/10.1029/2022MS002998 by Cochrane France, Wiley Online Library on [21/11/2022]. See the Terms and Conditions (https://onlinelibrary.wiley.com/terms-and-conditions) on Wiley Online Library for rules of use; OA articles are governed by the applicable Creative Commons License

Equi-temperature metamorphism (ETM), also referred to as isothermal metamorphism, occurs in snow in quasi-isothermal conditions and is driven by curvature gradients at the ice-air interfaces. Low-curvature ice surfaces have a lower saturation water vapor density than the high-curvature ones. Those curvature gradients lead thus to gradients of saturation vapor density, causing vapor transfer across the pores (e.g., diffusion) as well as phase changes (sublimation and deposition). Ice sublimates in higher curvature surfaces while water vapor deposits on lower curvature surfaces. The overall structure of snow gets rounder, coarser, and more sintered (see, e.g., Colbeck, 1980). These morphological changes come together with mechanical grain rearrangement, leading to snow settling. The resulting type of snow is referred to as rounded grains (RG) by *The International Classification for Seasonal Snow on the Ground* (Fierz et al., 2009). Equi-temperature metamorphism is constantly taking place in snow but at different levels of intensity. The higher the contrast in curvature and the higher the snow temperature, the more active the equi-temperature metamorphism. In the presence of high-temperature gradients, the influence of curvature effects becomes insignificant as the effect of the temperature gradient metamorphism (TGM) predominates.

Modeling the physical processes of metamorphism at a fine scale requires the description of the snow microstructure and its evolution (moving interfaces) as well as water vapor transport across the microstructure. Models can be applied on simplified geometry as in the work of Miller et al. (2003) who considered a 2D regular network of spherical grains. They can also take as input real snow microstructures, for example, 3D images of elementary representative volumes (REV) of snow obtained from micro-tomography (μCT). To enable microscale 3D modeling, different hypotheses can be used, describing kinetics at the interface with or without vapor diffusion and settling. Flin et al. (2003) considered a fully curvature-driven ETM based on the kinetic limited assumption and simulated it with an iterative method on 3D tomographic images. Comparisons between modeled and experimental microstructures were also shown. Also, a first simple grain rearrangement model was used to account for settling (Flin, 2004). Similarly, Vetter et al. (2010) used a Monte Carlo algorithm to simulate the isothermal metamorphism with the kinetic limited assumption and implemented a simple settling model. They obtained consistent results with observations although the model relies on a systematic parameter determination.

Recently, phase-field models have been developed to handle the numerical complexity of 3D microscale models (Bretin et al., 2019; Demange et al., 2017a, 2017b; Granger, 2019; Kaempfer & Plapp, 2009). Kaempfer and Plapp (2009) suggested a phase-field model for snow metamorphism considering interface kinetics and diffusion. They were pioneers with the phase-field method applied to snow metamorphism, and their results are consistent with observations. However, 3D evaluations are qualitative and limited only to one temperature gradient case mainly because of the numerical cost of the model. Subsequently, Demange et al. (2017a) and Granger (2019) introduced faceting effects in the modeling of individual snow crystals, providing very realistic shapes for high supersaturation conditions. For the scope of this study, ETM is simulated with a kinetic limited approach using the model of Bretin et al. (2019), a very efficient phase-field multiphase growth model for curvature-driven interface evolution. The model focuses on the principal process of driving ETM to avoid modeling several phenomena acting at different time scales, which requires a very small time step and a fine mesh. This enables running simulations with large 3D images as input, which is necessary to reach representative volumes of physical and microstructural properties.

Modeling the physics of snow growth classically relies on a condensation parameter α, also called attachment, deposition, or kinetic coefficient (e.g., Demange et al., 2017b; Flin et al., 2003; Furukawa, 2015; Granger et al., 2021; Harrington et al., 2019; Kaempfer & Plapp, 2009; Krol & Loewe, 2016; Libbrecht, 2005; Yokoyama & Kuroda, 1990). This parameter embodies the physics that governs how water molecules are incorporated into the ice lattice and is thus a key to model metamorphism. The α coefficient ranges from 0 to 1. One can think of α as a sticking probability, equal to the probability that a water vapor molecule striking the ice surface becomes assimilated into the crystal lattice (see, e.g., Furukawa, 2015; Libbrecht, 2005). However, it is still poorly understood and quantified notably because of its complex dependencies on temperature, humidity, and crystalline orientation (see, e.g., Libbrecht, 2019). Numerous values can be found in the literature, usually ranging from 10^{-4} to 10^{-1} (see, e.g., Libbrecht & Rickerby, 2013). The large uncertainty of this coefficient is one of the main limiting factors for the accuracy of metamorphism models.

To evaluate 3D models, simulated images are usually compared to experimental data through microstructural properties that can be calculated on 3D microstructures. Specific surface area (SSA), growth speed, ice thickness, and mean curvature were used in previous studies (Flin et al., 2003; Kaempfer & Plapp, 2009; Vetter et al., 2010).

19422466, 2022, 9, Downloaded from https://agupubs.onlinelibrary.wiley.com/doi/10.1029/2022MS002998 by Cochrane France, Wiley Online Library on [21/11/2022]. See the Terms and Conditions (https://onlinelibrary.wiley.com/terms-and-conditions) on Wiley Online Library for rules of use; OA articles are governed by the applicable Creative Commons License

To characterize the anisotropy of the microstructure, an anisotropy ratio was suggested based on the ratio of the horizontal and vertical covariance lengths (Calonne, Flin, et al., 2014; Löwe et al., 2013). Distributions of the mean curvature can be computed for the upward-facing and downward-facing ice surfaces, which can be interesting to identify faceted crystals and depth hoar (Calonne, Flin, et al., 2014).

Microscale models can be useful to design larger scale models notably to obtain regressions to predict macroscopic mechanical and physical properties. Estimating those properties is often based on numerical computations from experimentally obtained tomographic snow images (e.g., Calonne et al., 2011; Calonne, Flin, et al., 2014; Courville et al., 2010; Kaempfer et al., 2005; Srivastava et al., 2010). However, obtaining experimental images covering the wide range of scenarios of snow evolution encountered in nature is a challenge as it is time consuming. 3D microscale models of snow metamorphism could be a more efficient method as those properties can be estimated on simulated images.

In this article, we intend to go further in the microscale modeling of ETM by applying the efficient phase-field algorithm of Bretin et al. (2019) on tomographic images of snow and by calibrating it through the condensation coefficient α at -2°C using a temporal series of images obtained at this temperature. Thanks to the calibrated model, we investigated the evolution of both microstructural and macroscale transport properties computed on simulated images. Good agreements are reported when comparing the simulations to an independent data set of ETM at -2°C as well as to common estimates of the literature.

The paper is organized as follows. The physics of ETM and the phase-field description of the model are described in Section 2. The model calibration and an overview of the tools used for snow analysis are also presented in this section. Evaluation of the calibrated model and ETM prediction for different snow microstructures are investigated in Section 3. Section 4 discusses the model artifacts and the different results of the paper. Finally, Section 5 concludes the manuscript.

2. Method

2.1. Model

The phase-field model of Bretin et al. (2019) simulates a multiphase medium evolving under mean curvature flow and volume conservation of each phase. This flow is defined by an interface evolution where the normal velocity v_n is proportional to the local interface curvature C. In our case, we consider two phases where the model minimizes local curvatures while conserving the average of the sample mean curvature, which is equivalent to mass conservation of the ice phase (see, e.g., Bullard, 1997). The morphological transformations induced by the mean curvature flow can be interpreted as "smoothing" surfaces and are typically well-suited to model ETM as it is based on the same mathematical description. We apply the model of Bretin et al. (2019) to ETM for which, by definition, the temperature is isotropic and constant. Such a model implies that we assume kinetic-limited metamorphism: vapor transport in the pore space is not described. The vapor diffusion is indeed considered sufficiently fast, so that the vapor density far from the interface Γ is taken as constant and corresponds to the average sample mean curvature. Finally, the model does not include any mechanics and the settling of the ice grains is thus not represented here.

Under those conditions, ETM is classically described by the set of equations that follows (see, e.g., Flin et al., 2003; Kaempfer & Plapp, 2009). All the variables, together with the values and units used, are presented in Table 1.

$$v_n = \alpha v_{\text{kin}} \frac{\rho_{vs}^{\text{amb}} - \rho_{vs}^{\Gamma}}{\rho_{vs}^{\Gamma}} \quad \text{on } \Gamma \tag{1a}$$

$$\text{with } v_{\text{kin}} = \frac{\rho_{vs}^{\text{ref}}}{\rho_i} \sqrt{\frac{kT}{2\pi m}} \tag{1b}$$

$$\rho_{vs}^{\text{amb}} = \rho_{vs}^{\text{ref}}\, e^{2d_0 C^{\text{amb}}} \tag{2a}$$

$$\rho_{vs}^{\Gamma} = \rho_{vs}^{\text{ref}}\, e^{2d_0 C} \quad \text{on } \Gamma \tag{2b}$$

Equation 1 is the Hertz-Knudsen equation that describes the normal growth velocity v_n at the interface, such as positive values indicate ice growth and inversely, negative values indicate ice sublimation. The growth velocity is

19422466, 2022, 9, Downloaded from https://agupubs.onlinelibrary.wiley.com/doi/10.1029/2022MS002998 by Cochrane France, Wiley Online Library on [21/11/2022]. See the Terms and Conditions (https://onlinelibrary.wiley.com/terms-and-conditions) on Wiley Online Library for rules of use; OA articles are governed by the applicable Creative Commons License

Table 1
Notations and Values of the Physical Parameters (Above) and Variables Used in the Model (Below)

Symbol	Description	Value, unit	Reference
a	Mean intermolecular spacing in ice	3.19×10^{-10} m	Petrenko and Whitworth (1999)
k	Boltzmann's constant	1.38×10^{-23} J K^{-1}	
m	Mass of a water molecule	2.99×10^{-26} kg	Petrenko and Whitworth (1999)
λ	Interfacial free energy of ice	1.09×10^{-1} J m^{-2}	Libbrecht (2005)
ρ_i	Density of ice	917 kg m^{-3}	
T	ETM temperature	−2°C	
α	Condensation coefficient	$(9.8 \pm 0.7) \times 10^{-4}$	
n	Number of model time steps	4 to 11	
t_{step}	Model time step	0.5 to 8	
ε	Interface sharpness parameter	3 voxels	Denis (2015)

driven by the difference between the ambient saturation vapor density in the pores ρ_{vs}^{amb} and the saturation vapor density at the interface ρ_{vs}^{Γ}. We see in this equation that the interface growth velocity, thus the ETM rate, depends linearly on the condensation coefficient α.

Equations 2a and 2b correspond to the Gibbs-Thomson (Kelvin) relationship and describe the dependency of saturation vapor density with curvature at a given temperature using the capillary length $d_0 = \lambda a^3/(kT)$ (m) (Kaempfer & Plapp, 2009). Here, Equation 2a is used to describe the ambient saturation vapor density in the pores ρ_{vs}^{amb} in equilibrium, corresponding to the "ambient" curvature C^{amb}, defined as the average mean curvature of the entire snow volume. Equation 2b expresses the interface saturation vapor density ρ_{vs}^{Γ} in equilibrium with the local ice surface of curvature C. Both equations require a reference value of saturation vapor density ρ_{vs}^{ref} in air above a flat ice surface (i.e., where curvature is zero) and at a given temperature. The latter has been largely studied and can be determined as a function of the temperature using existing parameterizations. Here, we use the formulation of Goff and Gratch (1946), which is appropriate for our range of temperatures. Its expression can be found in Murphy and Koop (2005). Finally, let us remark that by injecting Equations 2a and 2b into Equation 1, and when considering curvatures close to C^{amb}, the relation can be written as $v_n = -2d_0\alpha v_{kin}C$.

The mean curvature flow model of Bretin et al. (2019) is solved with the phase-field method, which enables an implicit description of the interface using a function that varies smoothly between different phases. When adapted and applied to ETM with two phases, air and ice, the classical phase-field equation can be expressed as

$$\frac{\partial u}{\partial t}(x,t) = d_0\alpha v_{\text{kin}}\left(\Delta u(x,t) - \frac{1}{\varepsilon^2}W'(u)\right) \tag{3}$$

with x the position, t the time, $u(x, t)$ the phase function, ε the interface sharpness parameter, and W a double-well potential $W(s) := s^2(1-s)^2/2$. In the phase-field method, the interface Γ is the level set of value 1/2 of a phase function $u(x, t)$, which is defined from the distance function $d(x, t)$ to the interface Γ: $u(x, t) := u(d(x, t)/\varepsilon)$. In the sharp interface limit, it can be shown that Equation 3 can be matched to the sharp interface conditions, including the Gibbs-Thomson equation:

$$\frac{\partial d}{\partial t}(x,t) = -v_n = d_0\alpha v_{\text{kin}}\Delta d(x) \tag{4}$$

where $\Delta d(x) = 2C$ (see, e.g., Bullard, 1997).

Following Bretin et al. (2019), the canonical dimensionless form of Equation 3, based on the well-known Allen-Cahn equation, can be expressed as

$$\frac{\partial \tilde{u}}{\partial \tilde{t}}\left(\tilde{x},\tilde{t}\right) = \Delta\tilde{u}\left(\tilde{x},\tilde{t}\right) - \frac{1}{\tilde{\varepsilon}^2}W' + \tilde{\mu}\frac{1}{\tilde{\varepsilon}}\sqrt{2W\left(\tilde{u},\tilde{t}\right)} \tag{5}$$

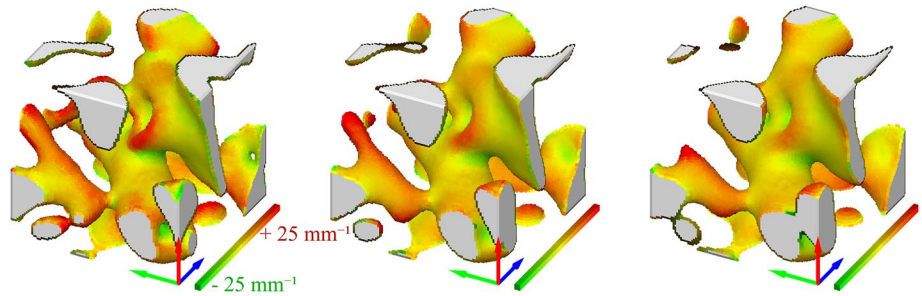


Figure 1. 3D representation of a tomographic snow sample from Hagenmuller et al. (2019) under the ETM model Snow3D after 0, 8, and 16 days at −2°C. See Section 2.2 for the correspondence between the simulation time and the physical time in days. Concave surfaces are shown in green, convex surfaces in red, and flat surfaces in yellow. The side of each viewing cube amounts to 675 µm. The blue, green, and red arrows, respectively, correspond to the x, y, and z coordinate axes, and z pointing to the upward direction.

where

$$\tilde{t} = \frac{t\alpha v_{\text{kin}} d_0}{d_x^2}, \quad \tilde{x} = \frac{x}{d_x}, \quad \tilde{\varepsilon} = \frac{\varepsilon}{d_x} \tag{6}$$

with d_x (m) the input image resolution. In Equation 5, $\tilde{\mu}$ is a Lagrange multiplier weighted by $\sqrt{2W(\tilde{u},\tilde{t})}$, which has been added to ensure a volume conservation with an error of $O(\tilde{\varepsilon}^2)$. Under common assumptions (periodic or Neumann boundary conditions), it can be shown that the Lagrange multiplier is written as (Bretin et al., 2019)

$$\tilde{\mu} = \frac{1}{\tilde{\varepsilon}} \frac{\int_\Omega W'(\tilde{u},\tilde{t})\mathrm{d}\tilde{x}}{\int_\Omega \sqrt{2W(\tilde{u},\tilde{t})}\mathrm{d}\tilde{x}} \tag{7}$$

The resulting phase-field model, called Snow3D, takes as input a 3D binary image of snow microstructure, such as obtained from tomography, and provides as output a series of 3D binary images at different time steps of the simulation. This is illustrated in Figure 1, where the overall smoothing effect of the curvature-driven evolution can be observed; ice tends to sublimate on the high-curvature surfaces (red areas), whereas water vapor deposits on low-curvature surfaces (green areas). The setting parameters of the model are the time step t_{step}, the number of time steps n, and the interface sharpness parameter ε, which, respectively, control the time resolution, the total time span, and the spatial resolution of the simulation. Values taken for those parameters are given in Table 1.

Finally, corrections were necessary to limit some artifacts of the model. First, curvature estimates at the image boundaries can be erroneous due to the periodic boundary conditions applied on the images. To avoid uncertainties regarding that issue, the edges of the simulated images were cut off by a certain width (0.6 mm) prior to further analysis. Also, as the model does not account for gravity, simulations can lead to "floating" ice grains (see Flin et al., 2003; Vetter et al., 2010), especially for recent snow, which undergoes significant settling (see, e.g., Flin et al., 2004; Schleef et al., 2014). To prevent this nonphysical phenomenon, we restrict input images to adequate snow microstructures and suppress disconnected ice grains.

2.2. Calibration

The model output is a series of n images separated by a time step t_{step} without any notion of physical duration. To obtain physical simulation evolution, a calibration step is thus needed. Considering the nondimensional time used to deduce the dimensionless Equation 5, the model physical time is expressed as (Equation 6)

$$t = \frac{\tilde{t}\, d_x^2}{\alpha v_{\text{kin}} d_0} \tag{8}$$

with t the physical time (s) and $\tilde{t} = t_{\text{step}} \times n$ the simulated time (−). The condensation coefficient α is needed to determine the physical time. To derive a value of α, we reproduced the ETM experiment of Flin et al. (2004) with

19422466, 2022, 9, Downloaded from https://agupubs.onlinelibrary.wiley.com/doi/10.1029/2022MS002998 by Cochrane France, Wiley Online Library on [21/11/2022]. See the Terms and Conditions (https://onlinelibrary.wiley.com/terms-and-conditions) on Wiley Online Library for rules of use; OA articles are governed by the applicable Creative Commons License

19422466, 2022, 9, Downloaded from https://agupubs.onlinelibrary.wiley.com/doi/10.1029/2022MS002998 by Cochrane France, Wiley Online Library on [21/11/2022]. See the Terms and Conditions (https://onlinelibrary.wiley.com/terms-and-conditions) on Wiley Online Library for rules of use; OA articles are governed by the applicable Creative Commons License

Table 2
Experimental Time Series of Snow Images Used to Calibrate and Evaluate the Snow3D Model (Section 3.1) (Above) and Experimental Snow Images Taken as Input to Simulate ETM and Predict Snow Properties (Section 3.2) (Below)

Name	Metamorphism type	Resolution (μm)	Dimension (voxel)	Density (kg m^{-3})	Snow type
Iso[a]	84 days of ETM at −2°C (10 images)	4.9	512	158	PP → RG
Eboni[b]	4 days of ETM at −2°C (20 images)	7.5	450	212	DF/RG
I17[c]	Recent fallen snow	7.3	700	147	DF/RG
TG2[c]	After 16 days at 19 K m^{-1}	7	700	254	FC/DH
Grad3[d]	After 8 days at 100 K m^{-1}	10	600	372	DH
7G9m[e]	After 21 days at 43 K m^{-1}	9.7	950	314	DH

Note. Density values correspond to the value at the initial stage of the series (0 day). Snow types are the main types reported throughout the time series or, when separated by an arrow, are the initial and final types.
[a]Flin et al. (2004). [b]Hagenmuller et al. (2019). [c]Dumont et al. (2021). [d]Calonne et al. (2012); Coléou et al. (2001). [e]Calonne, Flin, et al. (2014).

the model and compared the simulated series of images with the experimental one (series Iso in Table 2a) using the SSA evolution. The SSA parameter was chosen because it has a typical evolution very sensitive to ETM, which is well documented in the snow community (see, e.g., Flin et al., 2004; Kaempfer & Schneebeli, 2007; Vetter et al., 2010).

The series of experimental images of Flin et al. (2004) is composed of 10 images showing snow at different times of its evolution during ETM at −2°C from 0 to 84 days. Each image was obtained by micro-tomography of a snow specimen sampled from a snow slab undergoing ETM. The first images of the series (Iso01, Iso03, and Iso04) were not considered in this paper as they correspond to fresh snow, which could lead to grain disconnection issues (Section 2.1). To calibrate the model, we used the images Iso05 (day 5), Iso08 (day 12), Iso11 (day 18), and Iso15 (day 33). The last three images of the series (Iso19, Iso21, and Iso23) were not selected for calibration as they are close in time to the end of the experiment and data are too few for relevant statistics when estimating α. Finally, the sides of each simulated image were cut off by a stripe of thickness equal to the size of two heterogeneities (0.6 mm) before the SSA calculation to avoid edge artifacts while keeping volumes larger than the REV, typically about 2.5 mm for SSA (see, e.g., Flin et al., 2011).

The calibration process is schematized in four steps in Figure 2. For each selected image of the experimental series taken successively as input:

1. We run the model with the same parameters ($n = 10$, $t_{\text{step}} = 16$, $\varepsilon = 3$) to obtain a simulated series composed of 10 images.
2. We calculate the SSA evolution on the simulated series (Figure 2b).
3. We fit the SSA of the simulated series (Figure 2b) to the SSA of the experimental series (Figure 2a) by adjusting the time axis. More precisely, we scale the simulation time to the experimental time such that simulated SSA matches experimental SSA best by minimizing the Root Mean Square Error (RMSE) between the two curves (Figure 2c).
4. We use the simulated time and the fitted physical time to derive a value of the condensation coefficient α through Equation 8.

The average condensation coefficient and standard deviation were calculated from the α coefficients obtained from the four images. The resulting condensation coefficient is $\alpha = (9.8 \pm 0.7) \times 10^{-4}$. As the condensation coefficient is strongly temperature dependent and the temperature condition of the experiment of Flin et al. (2004) used to calibrate is −2°C, the calibrated model can only be used to simulate ETM at this temperature. To evaluate the influence of α on the microstructural parameters, we calculated the variation of the microstructural parameters (SSA, covariance length, and mean curvature) as a function of α variation. In the range of the α derived from the different samples, the parameters only have a maximum alteration of 5%, which is small compared to the physical precision of those parameters.

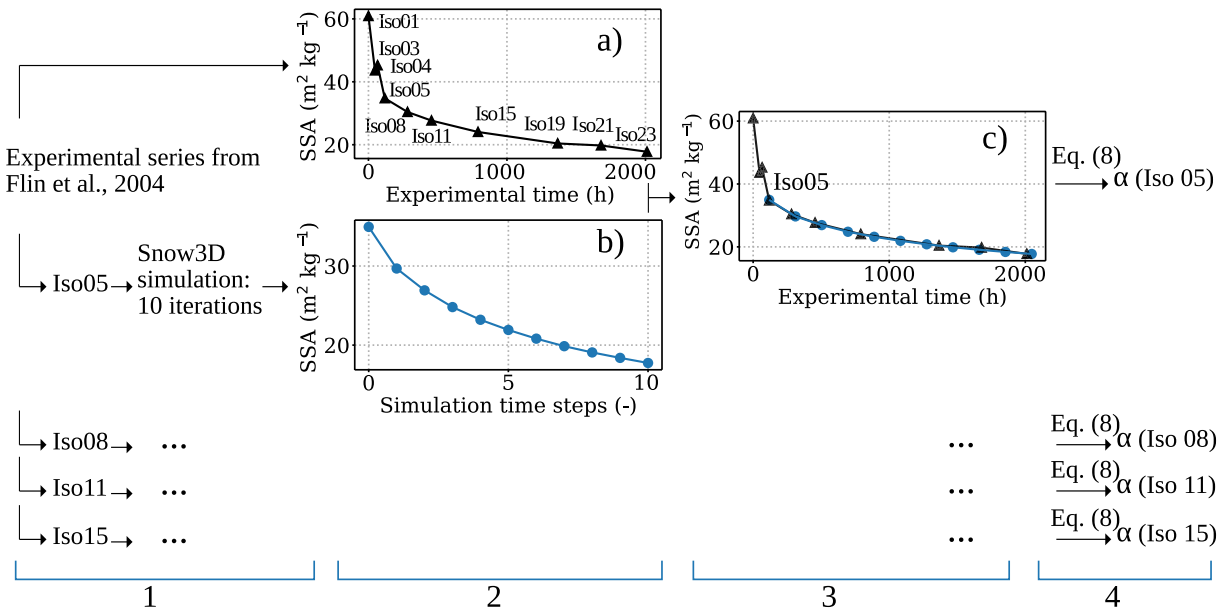


Figure 2. Workflow of the time calibration process and determination of the condensation coefficient.

2.3. Computation of Snow Properties

To characterize our simulated and experimental microstructures, we calculated on our volumes a range of microstructural and physical properties.

Microstructural properties:

- The snow density ρ_s (kg m^{-3}) was computed with a simple voxel counting algorithm.
- The mean curvature (mm^{-1}), defined as $(C_{\min} + C_{\max})/2$ with $C_{\min}$ and $C_{\max}$, respectively, the minimum and maximum 2D normal curvatures at a point of the surface, was obtained using the adaptive method proposed by Flin et al. (2004) (see also Calonne, Flin, et al. (2014); Flin et al. (2005) for additional information). As those values are computed for each point of the surface, they can be represented as statistical distributions. The mean curvature is thus expressed in terms of occurrence ratio, which gives the percentage of the ice surface area that exhibits a mean curvature located in a particular curvature class. Values near 0 mm^{-1} correspond to flat surfaces, positive values to convex surfaces, and negative values to concave surfaces; the higher the values, the more concave or convex the surfaces (see, e.g., Haffar et al., 2021; Ogawa et al., 2006).
- The specific surface area (SSA) (m^2 kg^{-1}), defined as the total surface area of ice per unit of mass, was computed using the voxel projection approach (Dumont et al., 2021; Flin et al., 2011).
- The covariance (or correlation) length l_c, which corresponds to the characteristic size of the ice heterogeneities in a given snow microstructure, was calculated along the x, y, and z directions of the images as in Calonne, Flin, et al. (2014) (see also Löwe et al., 2011).
- The anisotropy coefficient $\mathcal{A}(\star)$, which can be computed for each microstructural and physical property, was computed along the x, y, and z directions. This coefficient is defined as the ratio between the vertical component over the horizontal ones, such as $\mathcal{A}(\star) = \star_z/\star_{xy}$. The property is considered isotropic if it exhibits a coefficient close to 1; otherwise, the property is anisotropic. For example, $\mathcal{A}(l_c)$ largely above 1 means that the covariance length is higher in the vertical direction than in the horizontal one and thus describes a structure that is vertically elongated.

Macroscale transport properties: The 3D tensors of the intrinsic permeability **K** (m^2), of the effective thermal conductivity **k** (W m^{-1} K^{-1}), and of the effective coefficient of vapor diffusion **D** (m^2 s^{-1}) were computed on a set of simulated 3D images. For each property, a specific boundary value problem, arising from a homogenization technique (Auriault et al., 2009; Calonne, Geindreau, & Flin, 2015), is solved on the images applying periodic boundary conditions on the external boundaries of each volume using the software GeoDict (Thoemen et al., 2008). The effective diffusion coefficient was computed with an artificial diffusion coefficient of gas in

19422466, 2022, 9, Downloaded from https://agupubs.onlinelibrary.wiley.com/doi/10.1029/2022MS002998 by Cochrane France, Wiley Online Library on [21/11/2022]. See the Terms and Conditions (https://onlinelibrary.wiley.com/terms-and-conditions) on Wiley Online Library for rules of use; OA articles are governed by the applicable Creative Commons License

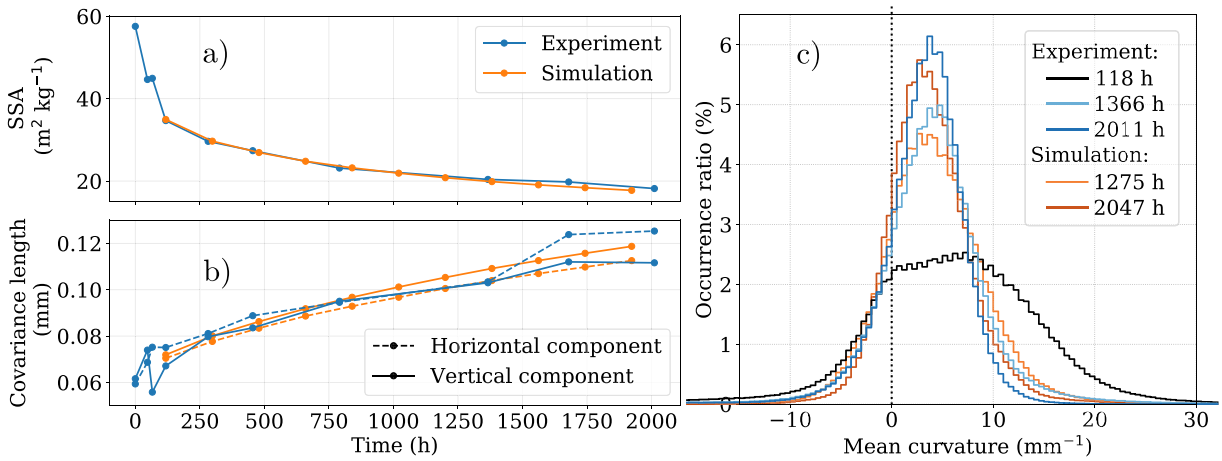


Figure 3. Comparison between the experiment of Flin et al. (2004) and the simulations, taking the Iso05 sample as the model input. Time evolution of (a) the SSA, (b) the covariance lengths, and (c) the mean curvature distribution. The black curve is the sample mean curvature distribution taken as an input of the model.

free air set to $D^{\text{air}}_{\text{artif}} = 1\ \text{m}^2\ \text{s}^{-1}$. In this study, we thus present the normalized values of the effective diffusion $\mathbf{D}/D^{\text{air}}$ (dimensionless). $\mathbf{K}$ is normalized by the equivalent sphere radius $r_{\text{es}} = 3/(\text{SSA} \times \rho_{\text{i}})$ to introduce a dimensionless tensor: $\mathbf{K}^* = \mathbf{K}/r_{\text{es}}^2$ (Calonne et al., 2012). As the nondiagonal terms of the tensors $\mathbf{K}$, $\mathbf{k}$, and $\mathbf{D}$ are negligible, we consider only the diagonal terms, that are seen as the eigenvalues of the tensors (the image axes x, y, and z are the principal directions of the microstructure, z being along the direction of gravity). Besides, the tensors are transversely isotropic as the components in x are very similar to the ones in y. In the following, K, k, and D refer to the average of the diagonal terms of $\mathbf{K}$, $\mathbf{k}$, and $\mathbf{D}$, respectively. K_z, k_z, and D_z refer to the vertical components and K_{xy}, k_{xy}, and D_{xy} refer to the mean horizontal components, where $K_{xy} = (K_x + K_y)/2$, $k_{xy} = (k_x + k_y)/2$, and $D_{xy} = (D_x + D_y)/2$. Finally, the anisotropy of the properties is characterized based on the anisotropy ratio $\mathcal{A}(\mathbf{K}) = K_z/K_{xy}$, $\mathcal{A}(\mathbf{k}) = k_z/k_{xy}$ and $\mathcal{A}(\mathbf{D}) = D_z/D_{xy}$ (see, e.g., Calonne, Flin, et al., 2014).

3. Results

3.1. Model Evaluation

Here, we evaluate the calibrated model by comparing experiments and simulations. To do so, we use the experimental series of images of Flin et al. (2004), which was the data set used to calibrate the model (Section 2.2), as well as the one of Hagenmuller et al. (2019) to allow for an independent comparison. Evaluations are performed through the SSA, the covariance lengths, and the mean curvature distribution computed from the simulated and experimental images.

The experimental series of images of Hagenmuller et al. (2019) was obtained as part of a study on dust particles in snow under both temperature gradient and equi-temperature conditions. Here, we focus on the equi-temperature part of the experiment and select 20 tomographic images from about 70 hr of ETM at −2°C (Eboni in Table 2a). We assume that dust has little influence on ETM (dust concentration of 0.5 mg g^{-1}) and artificially convert voxels of dust particles to voxels of air in the images so that we can use them as model inputs. In the work of Hagenmuller et al. (2019), the snow sample was observed with in operando X-ray tomography, meaning that the same sample was scanned at regular intervals (Calonne, Flin, et al., 2015). This method enables to compare directly simulated and experimental images, unlike the series of Flin et al. (2004), for which each image corresponds to a different snow sample.

The evolution of SSA, covariance lengths, and mean curvature from the experiment of Flin et al. (2004) and simulated with Snow3D is shown in Figure 3. As expected, the simulation follows closely the SSA decrease reported in the experiment (Figure 3a). The RMSE is of 0.58 $\text{m}^2\ \text{kg}^{-1}$ when comparing simulated and experimental SSA with values evolving from 35 to 18 $\text{m}^2\ \text{kg}^{-1}$. Covariance lengths increase over time from around 0.07 to 0.12 mm. This evolution is well reproduced by the model with a small RMSE of 0.006 mm (Figure 3b). Looking in more detail at the end of the time range of the experimental curve, the snow microstructure gets slightly elongated in

19422466, 2022, 9, Downloaded from https://agupubs.onlinelibrary.wiley.com/doi/10.1029/2022MS002998 by Cochrane France, Wiley Online Library on [21/11/2022]. See the Terms and Conditions (https://onlinelibrary.wiley.com/terms-and-conditions) on Wiley Online Library for rules of use; OA articles are governed by the applicable Creative Commons License

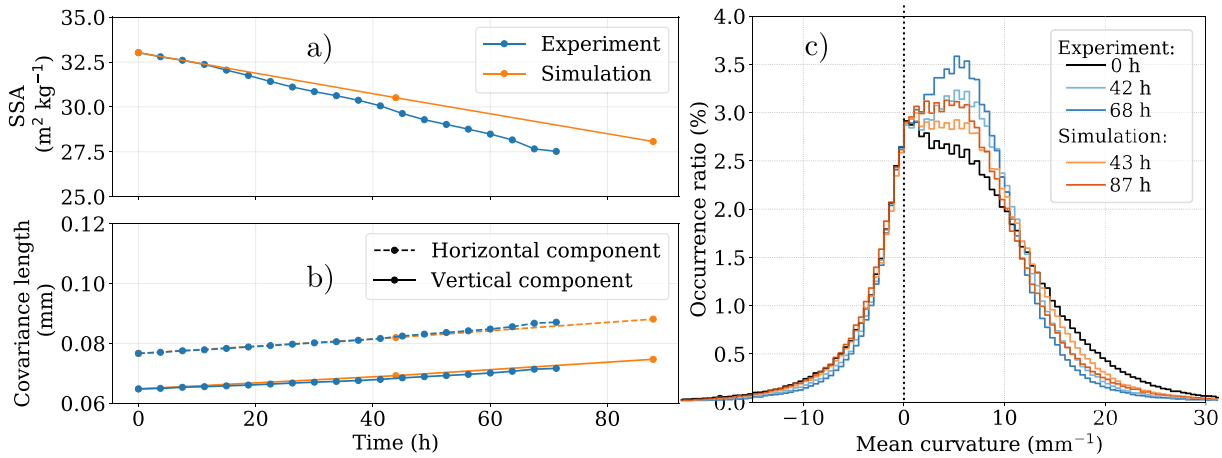


Figure 4. Comparison between the experiment of Hagenmuller et al. (2019) and the simulations. Time evolution of the (a) SSA, (b) covariance length, and (c) mean curvature distribution. The black curve is the sample mean curvature distribution taken as input of the model.

the horizontal direction with larger covariance lengths in the horizontal direction than in the vertical one. This evolution is probably inherent to the settling of the snow structure, but might be also partly due to the sampling protocol of the experiment (each image corresponds to a different sample). In the simulation, differences between vertical and horizontal covariance lengths do not exceed 0.005 mm and show a slight increase in time. This suggests an effect of the initial microstructure of the input sample on the evolution of the microstructural properties. The mean curvature distribution presented in Figure 3c allows to qualitatively compare the evolution of the ice-air interface morphology. We see that the distributions are narrowing and shifting toward lower mean curvature values, especially in the first time period. This depicts that ice surfaces are getting more uniform toward large rounded grains. Simulations follow closely the experimental data, showing good agreements at each time step. Finally, we should keep in mind that when evaluating the simulations against the data of Flin et al. (2004), the small disagreements observed might be partly due to the fact that the experimental properties do not only reflect time evolution but also the spatial variability of the monitored snow layer, and that they could be influenced by settling, which is not considered in simulations (see Section 2).

Figure 4 shows the model evaluation with the experiment of Hagenmuller et al. (2019). As this experiment is rather short compared to the previous one (70 hr), microstructural changes are more subtle. Overall, the SSA decreases from 33 to 28 m^2 kg^{-1}, whereas covariance length increases from 0.077 to 0.087 mm in the horizontal direction and from 0.065 to 0.072 mm in the vertical one. The model performs well for the SSA with an RMSE of 0.82 m^2 kg^{-1} and even better for the covariance length with an RSME of 0.0003 mm (mean for both directions). Here, we see that as in Figure 3, the ETM model depends on the initial microstructure with covariance lengths larger in the horizontal direction than in the vertical direction. The rate of SSA decrease seems slightly underestimated by the model, reaching a difference of 1.47 m^2 kg^{-1} after 80 hr; this is still small with respect to the SSA value range. The disparities between the experiment and the simulation on such a short period of time may be an effect of the differences between the experiment of Flin et al. (2004) and Hagenmuller et al. (2019) in terms of initial state, temperature, and humidity conditions. To obtain a good fit between the simulated SSA and the experimental SSA of Hagenmuller et al. (2019), a value of α of 13.1×10^{-4} should be taken. This value can give an idea of the sensibility of the SSA to α and is in the same order of magnitude as the calibrated one. Good agreements are overall found for the evolution of the mean curvature distribution (Figure 4c) with distributions centered around 5 mm narrowing with time. We can notice that the peak seems to narrow faster for the experiment than for the model, which is consistent with the experimental SSA decreasing faster than the modeled one, showing faster rounding of the ice surfaces.

3.2. Model Prediction

Here, the model is used to predict equi-temperature metamorphism on different snow microstructures. We selected four 3D experimental images of snow showing various features and used them as input images in the model. The samples are I17, TG2, Grad3, and 7G9m as presented in Table 2. The I17 sample corresponds to an

19422466, 2022, 9, Downloaded from https://agupubs.onlinelibrary.wiley.com/doi/10.1029/2022MS002998 by Cochrane France, Wiley Online Library on [21/11/2022]. See the Terms and Conditions (https://onlinelibrary.wiley.com/terms-and-conditions) on Wiley Online Library for rules of use; OA articles are governed by the applicable Creative Commons License

19422466, 2022, 9, Downloaded from https://agupubs.onlinelibrary.wiley.com/doi/10.1029/2022MS002998 by Cochrane France, Wiley Online Library on [21/11/2022]. See the Terms and Conditions (https://onlinelibrary.wiley.com/terms-and-conditions) on Wiley Online Library for rules of use; OA articles are governed by the applicable Creative Commons License

intermediate state between decomposed and fragmented particles and rounding grains (DF/RG) and presents an isotropic structure with rather rounded shapes. The TG2, Grad3, and 7G9m samples correspond to faceted crystals (FC) and depth hoar (DH); they underwent different temperature gradients and show the associated features in varying degrees (coarsening, faceting, striation, cup-shaped morphology, and structural anisotropy). The influence of ETM on snow types, such as depth hoar and faceted crystals, is interesting as in nature it is common for snow layers that underwent temperature gradient to be subject to periods of equi-temperature conditions. Simulations were performed considering isothermal conditions at −2°C and a condensation coefficient α of 9.8×10^{-4}. For each image, we obtained a simulated series of 4–11 images that reproduce 70–80 days of ETM in total. Figure 5 illustrates the simulated image series obtained for the four samples: a 3D view of the microstructure as well as a vertical slice are shown for each sample at the initial, intermediate, and final stages of the simulation.

3.2.1. Microstructural Parameters

Figure 6 presents the mean curvature distribution evolution for the samples I17 (DF/RG) and Grad3 (DH) (Section 2.3). For I17, the initial upward and downward distributions are similar with a peak of mean curvature located around 4 mm^{-1} and an occurrence ratio of 5% (Figure 6a). This reflects isotropic rounded ice structures at the initial stage. With time, the area-averaged mean curvature decreases gradually and the distributions are narrower, indicating that the ice structures tend toward larger rounded shapes and become more uniform.

For the evolution of Grad3 (Figure 6b), the initial upward and downward distributions are wider than for the initial stage of I17, revealing a larger variety of shapes. Besides, the initial upward and downward surfaces exhibit clearly distinct distributions: the peak of mean curvature is located around 0 mm^{-1} for the downward ones and at 1.5 mm^{-1} for the upward ones. The near-0 downward distribution depicts the presence of plane surfaces, which are facets as typically found in the lower area of a depth hoar crystal. In contrast, curvatures of the upward-looking surfaces show rather rounded shapes, again as typically observed in the upper area of a depth hoar crystal. With time, the differences between the downward and upward surfaces fade away and both show a narrower distribution (approx. 7% occurrence ratio) with a low area-averaged mean curvature. This indicates more uniform ice surfaces that are mostly large and rounded shapes for both downward and upward surfaces. This overall trend is similar to the one reported for I17.

Figure 7 shows the evolution of the SSA, covariance lengths, and structural anisotropy (anisotropy of covariance length) for our 4 simulated series. The SSA decreases exponentially for each image as classically reported for ETM experiments and microscale models of the literature (see, e.g., Kaempfer & Schneebeli, 2007; Vetter et al., 2010). Each series shows different decreasing rates and shapes, ranging from the exponential decrease from 23.7 to 9.2 $m^2\ kg^{-1}$ for the Grad3 sample to the almost linear slope from 20.6 to 13.7 $m^2\ kg^{-1}$ for the I17 sample. This difference in decrease rate can be explained by the initial microstructure. Grad3 shows a high initial SSA value, with sharp edges and facets, that leads to a quick and intense evolution (rounding) during the first stage of ETM. In contrast, the sample I17 presents rounded shapes in its initial stage. The covariance length evolution shows the characteristic increase observed during the ETM, reflecting the growth of snow grains and thus the overall increase in size of the microstructure (Calonne, Flin, et al., 2014; Löwe et al., 2011). Different evolution rates are again observed from an increase of 0.05 mm for I17 to 0.1 mm for Grad3. Finally, the evolution of the anisotropy ratio provides rather unexpected results. The samples I17 and TG2, presenting a rather isotropic structure with a ratio close to 1, show almost no changes over time. Samples that present a significant initial anisotropy, however, show an increase in their anisotropy with time. The anisotropy of Grad3 increases from 1.44 to 1.64 through the simulation and, in a lesser way, the anisotropy of 7G9m evolves from 1.24 to 1.27. By the end of the simulations, the covariance length of Grad3 is about two times larger in the vertical direction than in the horizontal direction. This increase in anisotropy can also be seen in the slices and 3D images in Figure 5: the initial vertically elongated ice structure is strengthened, leading to the development of vertical "columns" of ice (indicated by the black circles in Figure 5 and enlarged in the Supporting Information).

3.2.2. Macroscale Transport Properties

In this section, we present 3D estimates of macroscopic transport properties calculated on the images of the simulated series predicting ETM for the samples I17, TG2, 7G9m, and Grad3. We focus on the effective thermal conductivity, the normalized effective coefficient of vapor diffusion, and the dimensionless permeability (Section 2.3).

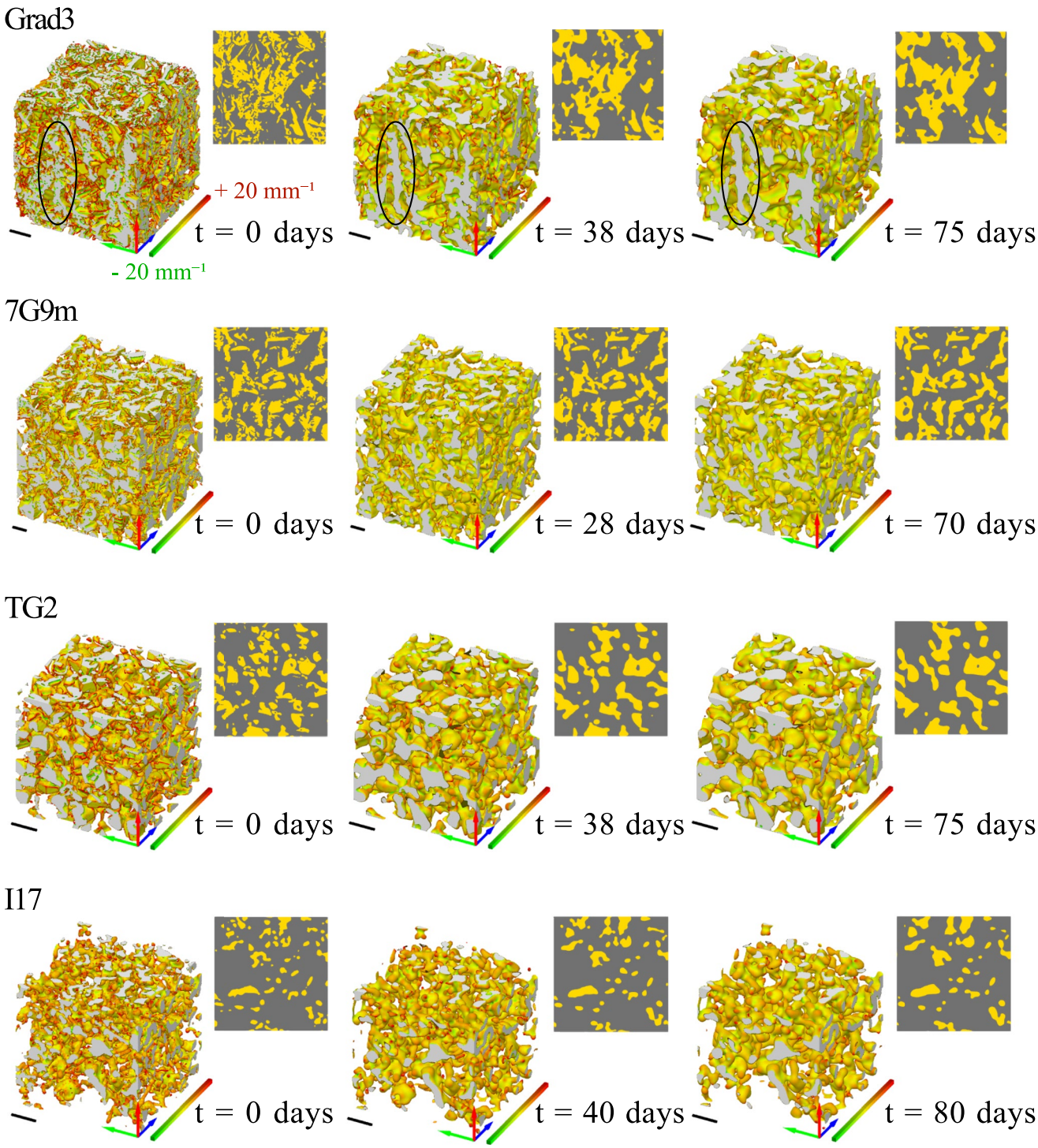


Figure 5. Initial, intermediate, and final stages of the simulated series of Grad3, 7G9m, TG2, and I17. 3D views and vertical slices taken at the center of each cube are presented. Concave surfaces are shown in green, convex surfaces in red, and flat surfaces in yellow in the 3D views. The ice phase is colored in yellow and the air phase in gray in the slice representations. Each scale bar represents 1 mm. The black circles highlight the formation of vertical columns for the Grad3 sample. Closer views are available in the supplemental materials.

Figure 8 presents the evolution of the transport properties with time for the samples I17 and Grad3. Density is also shown as the most impacting factor on those properties. For all properties, changes are rather small with time. For the lighter sample I17, the mean dimensionless permeability decreases from $10^{-0.33}$ to $10^{-0.43}$, conductivity increases from 0.078 to 0.081 W m^{-1} K^{-1}, and the normalized vapor diffusion decreases from 0.74 to 0.73.

19422466, 2022, 9, Downloaded from https://agupubs.onlinelibrary.wiley.com/doi/10.1029/2022MS002998 by Cochrane France, Wiley Online Library on [21/11/2022]. See the Terms and Conditions (https://onlinelibrary.wiley.com/terms-and-conditions) on Wiley Online Library for rules of use; OA articles are governed by the applicable Creative Commons License

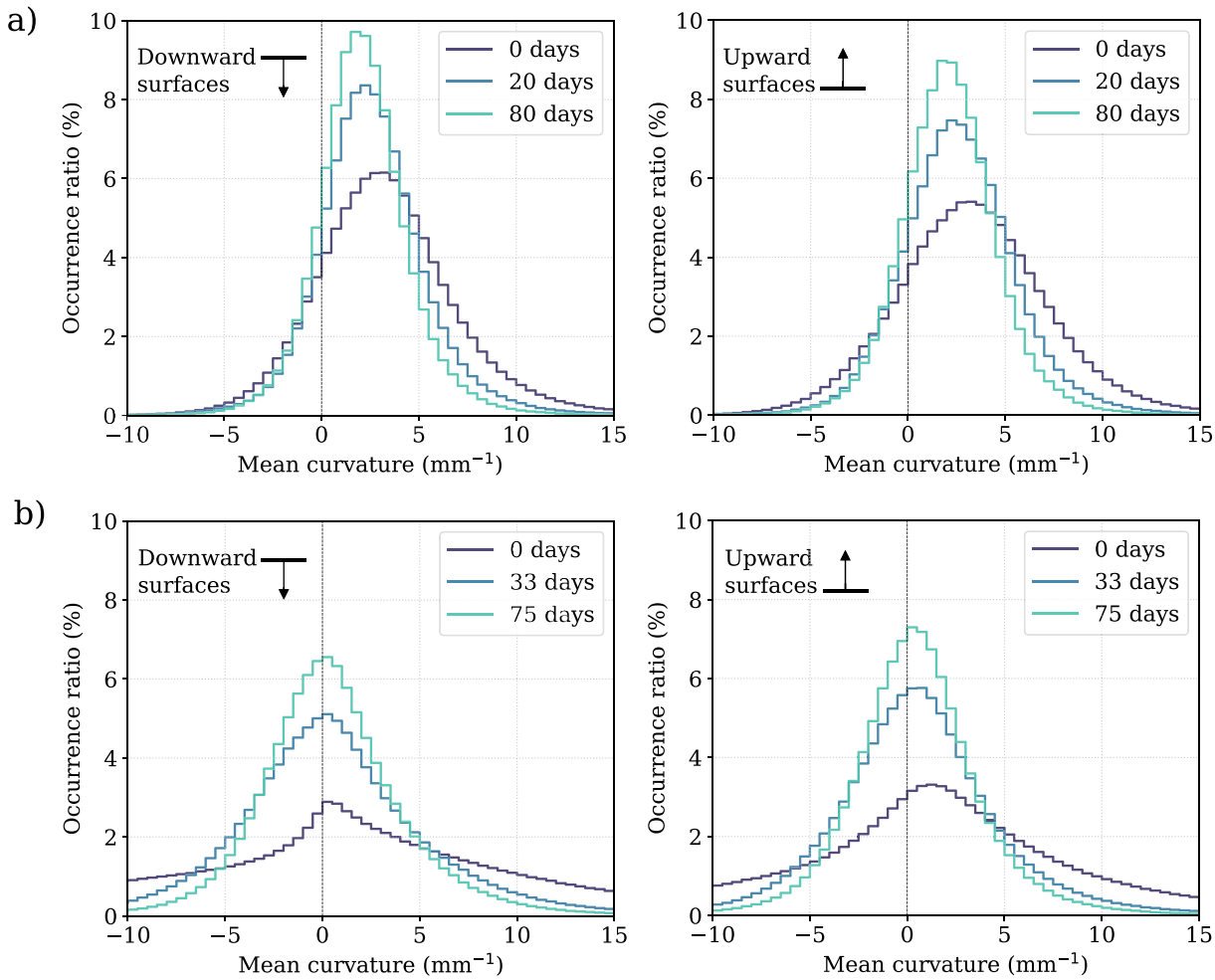


Figure 6. Time evolution of the mean curvature distribution from the downward (left) and upward (right) surfaces of I17 (a) and Grad3 (b) simulated series. Each curvature class is 0.5 mm^{-1} wide.

For the denser depth hoar sample Grad3, the mean dimensionless permeability decreases from $10^{-1.36}$ to $10^{-1.61}$, conductivity increases from 0.37 to 0.42 W m^{-1} K^{-1}, and the normalized vapor diffusion increases from 0.32 to 0.36. Looking at the directional components of the properties, a significant anisotropy is observed for the sample Grad3 (with a higher vertical component than the horizontal ones) compared to the I17 sample that is

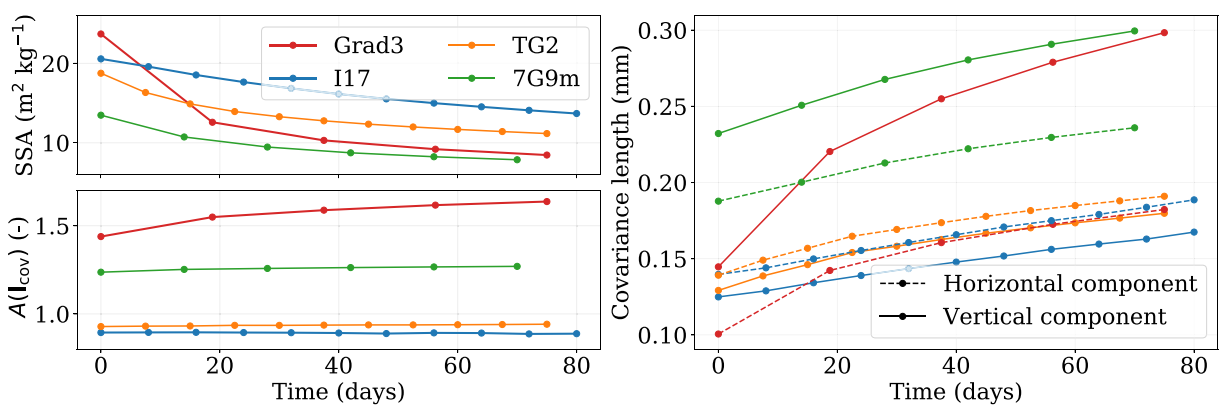


Figure 7. Time evolution of the microstructural parameters during simulations for the four snow microstructures.

19422466, 2022, 9, Downloaded from https://agupubs.onlinelibrary.wiley.com/doi/10.1029/2022MS002998 by Cochrane France, Wiley Online Library on [21/11/2022]. See the Terms and Conditions (https://onlinelibrary.wiley.com/terms-and-conditions) on Wiley Online Library for rules of use; OA articles are governed by the applicable Creative Commons License

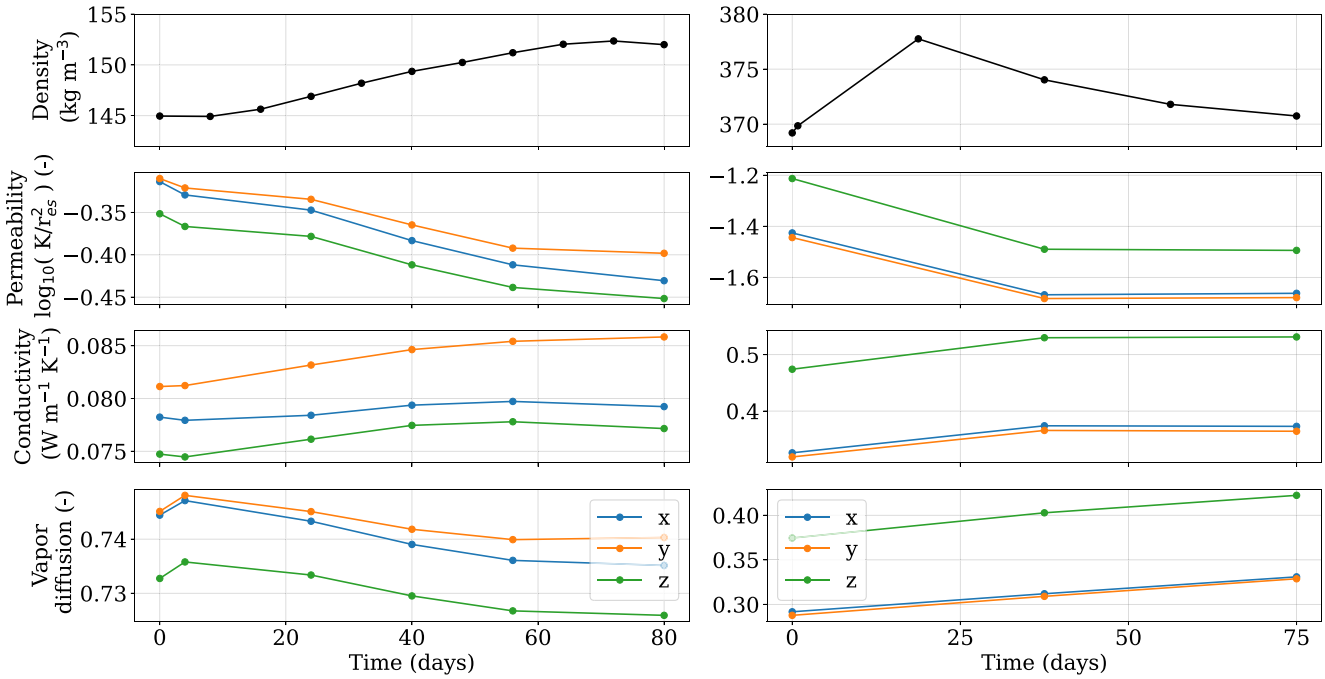


Figure 8. Time evolution of density, dimensionless permeability, effective thermal conductivity, and normalized effective coefficient of vapor diffusion for the simulated series of the I17 sample (left) and Grad3 sample (right).

rather isotropic. Some changes in transport properties can be related to the changes observed in density for both samples. Those density changes are unexpected as the model Snow3D is based on ice mass conservation. They correspond to artifacts that might come from a discretization effect of the phase-field function. For all the four simulated series, density changes are however small and comprised between 10 kg m^{-3} (3%) for the TG2 series and 4 kg m^{-3} (1%) for the Grad3 series as discussed in detail in Section 4.

Figure 9 shows the transport properties as a function of density. The tips and horizontal bars of the "T" markers represent, respectively, the vertical and horizontal components of the property, allowing to assess its anisotropy. The arrows indicate the evolution direction of the simulated series in time. The relative change τ of the mean property value between the initial and final stages is provided in the legend for each property. Finally, the computed transport properties are compared to estimates from analytical models and current regressions from literature (solid lines in Figure 9). We used the regression from Calonne et al. (2012) and Calonne et al. (2011), respectively, for permeability and thermal conductivity, both derived from data obtained from pore-scale computations on snow images spanning a wide range of seasonal snow types, and the self-consistent estimate "SC" for spherical inclusions (Auriault et al., 2009) for the coefficient of diffusion.

$$K_{\text{Calonne 2012}} = (3.0 \pm 0.3)\, {r_{es}}^2 \exp\left((-0.0130 \pm 0.0003)\, \rho_s\right) \tag{9a}$$

$$k_{\text{Calonne 2011}} = 2.5 \times 10^{-6} \rho_s^2 - 1.23 \times 10^{-4} \rho_s + 0.024 \tag{9b}$$

$$D_{\text{SC}} = 1 - \frac{3\rho_s}{2\rho_i} \tag{9c}$$

Overall, the temporal evolution of the different series in terms of macroscale properties and density, represented by the arrows and by the relative changes, τ, follows the reference parameterizations. Estimates of the effective coefficient of vapor diffusion for the samples Grad3 and 7G9m show however an opposite trend than the trend from the reference model, that is, we observe an increase with density and time instead of a decrease. This increase can be interpreted as an effect of the microstructure on the diffusion coefficient, different from the effect of density. Indeed, in Figure 9 of Calonne, Geindreau, and Flin (2014), we see that for a given density, effective vapor diffusion is smaller for depth hoar than for faceted crystals and even more for rounded grains. Following this study, the simulated evolution of the Grad3 and 7G9m samples from depth hoar to more rounded shapes

19422466, 2022, 9, Downloaded from https://agupubs.onlinelibrary.wiley.com/doi/10.1029/2022MS002998 by Cochrane France, Wiley Online Library on [21/11/2022]. See the Terms and Conditions (https://onlinelibrary.wiley.com/terms-and-conditions) on Wiley Online Library for rules of use; OA articles are governed by the applicable Creative Commons License

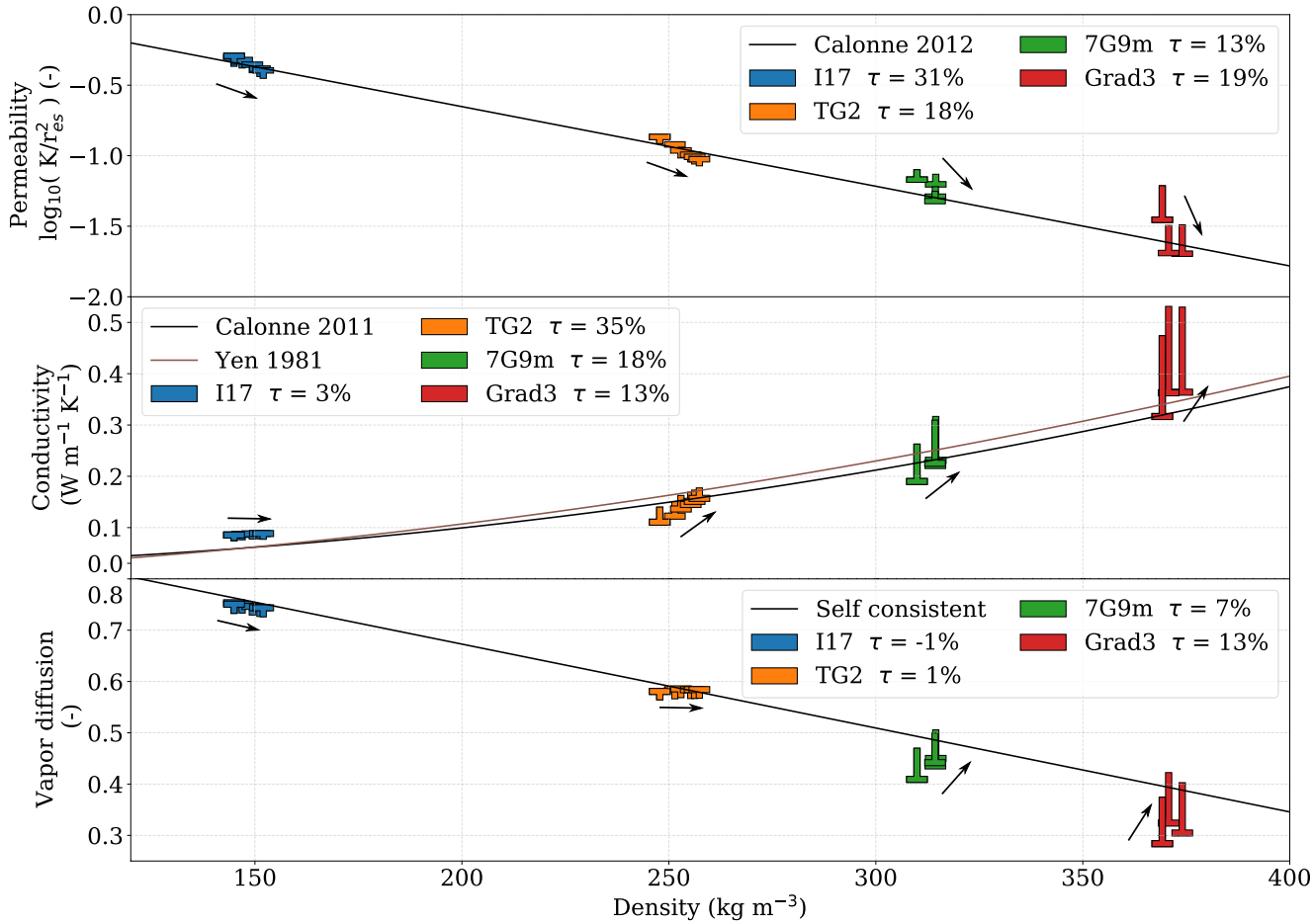


Figure 9. Effective thermal conductivity, normalized effective vapor diffusion, and dimensionless permeability as a function of density.

would favor diffusion. Hence, two opposite effects could be competing here and it seems that the influence of microstructure overcomes the one of density. The impact of microstructure is also present for the dimensionless permeability as reported in Figure 1 of Calonne et al. (2012) for example. In the latter figure, the dimensionless permeability decreases with increasing density; but, at a given density, depth hoar samples tend to exhibit higher dimensionless permeability than faceted crystals or rounded grains. For Grad3 and 7G9m, both the microstructure and the density evolution lead to a decreasing dimensionless permeability. For the thermal conductivity, the density changes seem to drive most of the evolution and the impact of the microstructural changes is not visible in our ETM simulation. The microstructural impact is however observed in the case of a TGM experiment in Calonne, Flin, et al. (2014) where thermal conductivity increases with time at constant density.

4. Discussion

Based on the phase-field approach of Bretin et al. (2019), the Snow3D model provides an effective way to simulate ETM from 3D tomographic images of real snow samples. This optimized model has been calibrated and evaluated using the experimental ETM series at −2°C and used to simulate metamorphism on a set of four snow microstructures. It can adequately predict the evolution with time of numerous microstructural parameters as well as macroscale transport properties.

Having the results in mind, it is worth discussing the model artifacts in some more details. For our four simulated image series, we observe a slight increase in density with time between 1% and 3% or from 4 to 10 kg m^{-3} (Figures 8 and 9). However, the model is based on ice mass conservation and does not simulate settling or any mechanical processes. Changes in density are thus artifacts, which seem to come from the binarization

19422466, 2022, 9, Downloaded from https://agupubs.onlinelibrary.wiley.com/doi/10.1029/2022MS002998 by Cochrane France, Wiley Online Library on [21/11/2022]. See the Terms and Conditions (https://onlinelibrary.wiley.com/terms-and-conditions) on Wiley Online Library for rules of use; OA articles are governed by the applicable Creative Commons License

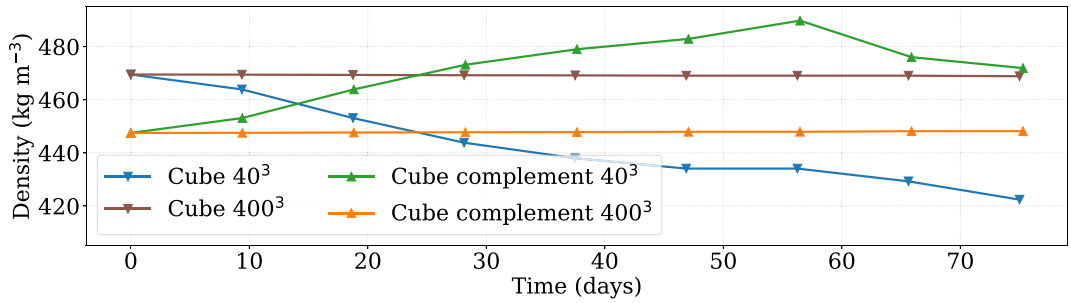


Figure 10. Influence of the image resolution on the modeled density evolution: an example of a cube surrounded by air and its complementary image as model inputs.

of the phase-field function. At the end of the simulation, the continuous interface of the phase-field function is approximated by air and ice voxels of finite length. This step can induce an error in the definition of the ice-air interface position of one voxel at most. The proportion of voxel defining the ice interface in the binarized images constitutes 9% of the total ice voxels for the TG2 sample and 6% for the Grad3 sample, which converted in mass corresponds indeed to the mass gain observed in the simulations. In Figure 10, we ran the model on four different images: a cube surrounded by air with a size of 40^3 voxels; the same cube with a size of 400^3 voxels; the complementary of the cube — a cube of air surrounded by ice — with a size of 40^3 voxels; and the same complementary image with a size of 400^3 voxels. The idea was to test the sensitivity of the simulated density to image resolution and interface shapes with an image presenting convex shapes (the ice cube surrounded by air) and one presenting concave shapes (the complementary air cube surrounded by ice). We see clearly in the figure that for the high resolution, the density is stable in time, whereas for the coarser resolution, the density shows an erratic evolution with changes of about 10%. Indeed, the higher the resolution, the thinner the layer of voxel of the ice surface, and the lower the error. In terms of the ratio between the object length (covariance length) and the voxel size, the 4 studied tomographies are similar to the cube and complementary cube of 40^3 voxels. Finally, the density artifact reported in our simulations (maximum of 3%) is lower than the precision of field density measurements, which is of the order of 5% (Proksch et al., 2016). Moreover, snow settling is an important process of ETM, for example, Flin et al. (2004) recorded, starting from fresh snow, a density increase of 60% in 80 days of ETM. Thus, the density artifacts are relatively small in comparison with the settling that can occur for recent natural snow.

It also seems important to discuss the model calibration and evaluation. In our calibration process, the condensation coefficient α is determined using the experimental time series of Flin et al. (2004) from an ETM experiment of 84 days at −2°C. A value of $(9.8 \pm 0.7) \times 10^{-4}$ was found, which is in the lower range of the values in the literature. When comparing measurements of α, it is important to consider the temperature and the supersaturation conditions. Unlike for crystals growing in the atmosphere, ETM in the snowpack is concerned by low supersaturations, typically of the order of 0.1%–0.01%, which results in low α values (see, e.g., Fig. 6 of Libbrecht and Rickerby (2013) or Fig. 4.24 of Libbrecht (2019)). The reported values of α are mostly found from experiments of ice crystals growing at high supersaturation (between 1% and 0.1%). For instance, in Libbrecht and Rickerby (2013), the lowest supersaturation measurements of crystals growing at −3°C indicate an α around 0.06 for a supersaturation of 0.1%. In Sei and Gonda (1989), at −2°C, α is measured around 0.15 for the growth of prismatic faces at a supersaturation of 0.5%. Earlier, Beckmann and Lacmann (1982) measured a mean condensation coefficient of 0.14 for a temperature varying between −7°C and −15°C at high supersaturation (above 0.5%). The wide range of α values available in the literature reflects the various and complex dependencies of this coefficient, which depends on temperature and water vapor supersaturation, but also on ice crystalline orientation (see, e.g., Granger et al., 2021; Libbrecht, 2019). In this work, simulations were performed for ETM metamorphism (i.e., for supersaturations close to 0.01%) with a constant and isotropic value of α determined for a temperature of −2°C. Such simulations are only valid at that temperature and adequate condensation coefficient values should be used when simulating ETM with the model at different temperatures. To test and evaluate the calibrated model, we used the experimental time series of Hagenmuller et al. (2019) of an ETM experiment also performed at −2°C. Very good agreements were found between simulation and experiment (Figure 4). As this time series is however rather short (3 days), the model evaluation would benefit from additional comparisons with longer time series of ETM, which is planned as a future work.

19422466, 2022, 9, Downloaded from https://agupubs.onlinelibrary.wiley.com/doi/10.1029/2022MS002998 by Cochrane France, Wiley Online Library on [21/11/2022]. See the Terms and Conditions (https://onlinelibrary.wiley.com/terms-and-conditions) on Wiley Online Library for rules of use; OA articles are governed by the applicable Creative Commons License

19422466, 2022, 9, Downloaded from https://agupubs.onlinelibrary.wiley.com/doi/10.1029/2022MS002998 by Cochrane France, Wiley Online Library on [21/11/2022]. See the Terms and Conditions (https://onlinelibrary.wiley.com/terms-and-conditions) on Wiley Online Library for rules of use; OA articles are governed by the applicable Creative Commons License

Finally, simulations with Snow3D pointed out the enhancement of the structural anisotropy of snow during ETM for the initially anisotropic snow sample Grad3 (depth hoar). This sample has a particular morphology: it presents a rather dense structure (about 370 kg m^{-3}) with many intricate angular shapes and with a preferential vertical elongation (initial anisotropy ratio of 1.4). Under the simulated ETM, the microstructure becomes smoother and small ice convexities and concavities disappear while larger ice structures strengthen, forming a vertically oriented ice network. Consequently, the structural anisotropy ratio increases up to 1.6 for the Grad3 sample. A similar analysis can be done for the sample 7G9m, for which the initial anisotropy is preserved throughout the simulation (ratio of about 1.25). The enhancement or conservation of the structural anisotropy during ETM, which was never reported in previous studies, is a rather unexpected result as one could have anticipated that the smoothing effect of the ETM would make the structural anisotropy disappear for the benefit of more isotropic structures as classically formed under equi-temperature conditions, such as rounded grains.

5. Conclusion

A snow ETM model based on the work of Bretin et al. (2019) was applied to snow images obtained by X-ray tomography to study the impact on the microstructural and transport properties. The model was calibrated to experimental data at –2°C by fitting the SSA of the series from Flin et al. (2004) to the simulation. A value of the condensation coefficient α was derived: $\alpha = (9.8 \pm 0.7) \times 10^{-4}$. The calibrated model was then evaluated with the independent experimental series of Hagenmuller et al. (2019) by looking at microstructural properties, such as the SSA, the covariance length, the structural anisotropy, and the mean curvature. As this evaluation yielded very encouraging results, the model Snow3D was used to predict ETM for four different snow microstructures from experimental samples. The four simulated time series were used to analyze microstructural parameters (SSA, covariance length, and structural anisotropy) and physical effective transport properties (thermal conductivity, vapor diffusivity, and permeability). Those results are in good agreement with current models and regressions. They also exhibit the influence of the microstructure on microscale (structural anisotropy) and macroscale (effective coefficient of diffusion) phenomena. For example, we observed an enhancement of the structural anisotropy in the case of initially anisotropic microstructures. It questions the idea that isotropic conditions systematically tend to remove the snow structure anisotropy. This model is a step forward for modeling ETM at the pore scale. Future studies will focus on implementing the settling process and water vapor transport in pores as well as extending the model to other metamorphism conditions, considering the condensation coefficient dependencies with temperature and grain orientation especially.

Data Availability Statement

The data generated and investigated in this article are available at https://zenodo.org/record/5865001 (DOI: https://doi.org/10.5281/zenodo.5865001) (Bouvet et al., 2022).

Acknowledgments
We thank the two anonymous reviewers for their constructive comments that improved the manuscript. We would like to thank Elie Bretin, Roland Denis, Jacques-Olivier Lachaud, and Edouard Oudet for developing the Snow3D phase-field model and sharing their code in the framework of the DigitalSnow project (ANR-11-BS02-009). We are also grateful to the 3SR tomographic plateform and the ESRF ID19 beamline for the acquisition of all the 3D images used in this study. CNRM/CEN members are also thanked for their help in the sampling, preparation, and acquisition processes of the snow images. The 3SR lab is part of the Labex Tec 21 (Investissements d'Avenir, Grant Agreement ANR-11-LABX-0030). CNRM/CEN is part of Labex OSUG@2020 (Investissements d'Avenir, Grant ANR-10-LABX-0056). This research has been supported by the MiMESis-3D ANR project (ANR-19-CE01-0009).

References

Auriault, J., Boutin, C., & Geindreau, C. (2009). *Homogenization of coupled phenomena in heterogenous media*. ISTE Ltd and John Wiley & Sons.

Beckmann, W., & Lacmann, R. (1982). Interface kinetics of the growth and evaporation of ice single crystals from the vapour phase: II. measurements in a pure water vapour environment. *Journal of Crystal Growth*, *58*(2), 433–442. https://doi.org/10.1016/0022-0248(82)90292-5

Bouvet, L., Calonne, N., Flin, F., & Geindreau, C. (2022). Snow equi-temperature metamorphism described by a phase-field model applicable on micro-tomographic images: Prediction of microstructural and transport properties [dataset]. Zenodo. https://doi.org/10.5281/zenodo.5865001

Bretin, E., Denis, R., Lachaud, J.-O., & Oudet, E. (2019). Phase-field modelling and computing for a large number of phases. *ESAIM: Mathematical Modelling and Numerical Analysis*, *53*(3), 805–832. https://doi.org/10.1051/m2an/2018075

Bullard, J. W. (1997). Numerical simulations of transient-stage Ostwald ripening and coalescence in two dimensions. *Materials Science and Engineering: A*, *238*(1), 128–139. https://doi.org/10.1016/S0921-5093(97)00439-5

Calonne, N., Flin, F., Geindreau, C., Lesaffre, B., & Rolland du Roscoat, S. (2014). Study of a temperature gradient metamorphism of snow from 3-D images: Time evolution of microstructures, physical properties and their associated anisotropy. *The Cryosphere*, *8*(6), 2255–2274. https://doi.org/10.5194/tc-8-2255-2014

Calonne, N., Flin, F., Lesaffre, B., Dufour, A., Roulle, J., Puglièse, P., et al. (2015). CellDyM: A room temperature operating cryogenic cell for the dynamic monitoring of snow metamorphism by time-lapse X-ray microtomography. *Geophysical Research Letters*, *42*(10), 3911–3918. https://doi.org/10.1002/2015GL063541

Calonne, N., Flin, F., Morin, S., Lesaffre, B., Rolland du Roscoat, S., & Geindreau, C. (2011). Numerical and experimental investigations of the effective thermal conductivity of snow. *Geophysical Research Letters*, *38*(23). https://doi.org/10.1029/2011GL049234

Calonne, N., Geindreau, C., & Flin, F. (2014). Macroscopic modeling for heat and water vapor transfer in dry snow by homogenization. *The Journal of Physical Chemistry B*, *118*(47), 13393–13403. https://doi.org/10.1021/jp5052535

Calonne, N., Geindreau, C., & Flin, F. (2015). Macroscopic modeling of heat and water vapor transfer with phase change in dry snow based on an upscaling method: Influence of air convection. *Journal of Geophysical Research: Earth Surface*, *120*(12), 2476–2497. https://doi.org/10.1002/2015JF003605

Calonne, N., Geindreau, C., Flin, F., Morin, S., Lesaffre, B., Rolland du Roscoat, S., & Charrier, P. (2012). 3-D image-based numerical computations of snow permeability: Links to specific surface area, density, and microstructural anisotropy. *The Cryosphere*, *6*(5), 939–951. https://doi.org/10.5194/tc-6-939-2012

Colbeck, S. C. (1980). Thermodynamics of snow metamorphism due to variations in curvature. *Journal of Glaciology*, *26*(94), 291–301. https://doi.org/10.3189/S0022143000010832

Colbeck, S. C. (1997). *A review of sintering in seasonal snow* (Vol. 97–10). Cold Regions Research and Engineering Laboratory. Retrieved from https://apps.dtic.mil/sti/citations/ADA335556

Coléou, C., Lesaffre, B., Brzoska, J.-B., Ludwig, W., & Boller, E. (2001). Three-dimensional snow images by X-ray microtomography. *Annals of Glaciology*, *32*, 75–81. https://doi.org/10.3189/172756401781819418

Courville, Z., Hörhold, M., Hopkins, M., & Albert, M. (2010). Lattice-Boltzmann modeling of the air permeability of polar firn. *Journal of Geophysical Research*, *115*(F4), F04032. https://doi.org/10.1029/2009JF001549

Demange, G., Zapolsky, H., Patte, R., & Brunel, M. (2017a). Growth kinetics and morphology of snowflakes in supersaturated atmosphere using a three-dimensional phase-field model. *Physical Review E - Statistical Physics, Plasmas, Fluids, and Related Interdisciplinary Topics*, *96*(2), 022803. https://doi.org/10.1103/PhysRevE.96.022803

Demange, G., Zapolsky, H., Patte, R., & Brunel, M. (2017b). A phase field model for snow crystal growth in three dimensions. *Npj Computational Materials*, *3*(1), 1–7. https://doi.org/10.1038/s41524-017-0015-1

Denis, R. (2015). Simulation multi-label phase-field. In *(oral presentation of the DigitalSnow ANR Project, meeting held in Autrans, 8th July 2015)*. Retrieved from https://projet.liris.cnrs.fr/dsnow/doc/Autrans-Juin2015/presentation-Roland-Denis.pdf

Dumont, M., Flin, F., Malinka, A., Brissaud, O., Hagenmuller, P., Lapalus, P., et al. (2021). Experimental and model-based investigation of the links between snow bidirectional reflectance and snow microstructure. *The Cryosphere*, *15*(8), 3921–3948. https://doi.org/10.5194/tc-15-3921-2021

Fierz, C., Armstrong, R. L., Durand, Y., Etchevers, P., Greene, E., McClung, D. M., et al. (2009). The international classification for seasonal snow on the ground. *IHP-VII Technical Documents in Hydrology, IACS Contribution n°1*, 83. Retrieved from https://unesdoc.unesco.org/ark:/48223/pf0000186462

Flin, F. (2004). *Snow metamorphism description from 3D images obtained by X-ray microtomography* (PhD. thesis), Université Grenoble 1. Retrieved from http://www.umr-cnrm.fr/cen/microstructure/these/flin_these_pdf.zip

Flin, F., Brzoska, J.-B., Coeurjolly, D., Pieritz, R., Lesaffre, B., Coleou, C., et al. (2005). Adaptive estimation of normals and surface area for discrete 3-D objects: Application to snow binary data from X-ray tomography. *IEEE Transactions on Image Processing*, *14*(5), 585–596. https://doi.org/10.1109/TIP.2005.846021

Flin, F., Brzoska, J.-B., Lesaffre, B., Coléou, C., & Pieritz, R. A. (2003). Full three-dimensional modelling of curvature-dependent snow metamorphism: First results and comparison with experimental tomographic data. *Journal of Physics D: Applied Physics*, *36*(10A), A49–A54. https://doi.org/10.1088/0022-3727/36/10A/310

Flin, F., Brzoska, J.-B., Lesaffre, B., Coléou, C., & Pieritz, R. A. (2004). Three-dimensional geometric measurements of snow microstructural evolution under isothermal conditions. *Annals of Glaciology*, *38*, 39–44. https://doi.org/10.3189/172756404781814942

Flin, F., Lesaffre, B., Dufour, A., Gillibert, L., Hasan, A., Rolland du Roscoat, S., et al. (2011). On the computations of specific surface area and specific grain contact area from snow 3D images. In Y. Furukawa (Ed.), *Proceedings of the 12th international conference on the physics and chemistry (PCI 2010) of ice held at sapporo* (pp. 321–328) on 5-10 September 2010. Retrieved from http://www.umr-cnrm.fr/IMG/pdf/flin_etal_2011_ssa_sgca_published_color.pdf

Furukawa, Y. (2015). 25 - Snow and ice crystal growth. In T. Nishinaga (Ed.), *Handbook of crystal growth* (2nd ed., pp. 1061–1112). Elsevier. Retrieved from https://www.sciencedirect.com/science/article/pii/B9780444563699000253

Goff, J., & Gratch, S. (1946). Low-pressure properties of water from -160 to 212 F. *Transactions of the American society of heating and ventilation engineers*, *52*, 95–122.

Granger, R. (2019). *Crystal growth physics in dry snow metamorphism: Characterisation and modeling of kinetics effects*. PhD. Thesis, Université Grenoble Alpes (ComUE). Retrieved 2020-06-09, from https://tel.archives-ouvertes.fr/tel-03092266

Granger, R., Flin, F., Ludwig, W., Hammad, I., & Geindreau, C. (2021). Orientation selective grain sublimation–deposition in snow under temperature gradient metamorphism observed with diffraction contrast tomography. *The Cryosphere*, *15*(9), 4381–4398. https://doi.org/10.5194/tc-15-4381-2021

Haffar, I., Flin, F., Geindreau, C., Petillon, N., Gervais, P.-C., & Edery, V. (2021). X-ray tomography for 3D analysis of ice particles in jet A-1 fuel. *Powder Technology*, *384*, 200–210. https://doi.org/10.1016/j.powtec.2021.01.069

Hagenmuller, P., Flin, F., Dumont, M., Tuzet, F., Peinke, I., Lapalus, P., et al. (2019). Motion of dust particles in dry snow under temperature gradient metamorphism. *The Cryosphere*, *13*(9), 2345–2359. https://doi.org/10.5194/tc-13-2345-2019

Hammonds, K., Lieb-Lappen, R., Baker, I., & Wang, X. (2015). Investigating the thermophysical properties of the ice–snow interface under a controlled temperature gradient: Part I: Experiments & observations. *Cold Regions Science and Technology*, *120*, 157–167. https://doi.org/10.1016/j.coldregions.2015.09.006

Harrington, J. Y., Moyle, A., Hanson, L. E., & Morrison, H. (2019). On calculating deposition coefficients and aspect-ratio evolution in approximate models of ice crystal vapor growth. *Journal of the Atmospheric Sciences*, *76*(6), 1609–1625. https://doi.org/10.1175/JAS-D-18-0319.1

Kaempfer, T. U., & Plapp, M. (2009). Phase-field modeling of dry snow metamorphism. *Physical Review E*, *79*(3), 031502. https://doi.org/10.1103/PhysRevE.79.031502

Kaempfer, T. U., & Schneebeli, M. (2007). Observation of isothermal metamorphism of new snow and interpretation as a sintering process. *Journal of Geophysical Research*, *112*(D24), D24101. https://doi.org/10.1029/2007JD009047

Kaempfer, T. U., Schneebeli, M., & Sokratov, S. (2005). A microstructural approach to model heat transfer in snow. *Geophysical Research Letters*, *32*(21), L21503. https://doi.org/10.1029/2005GL023873

Krol, Q., & Loewe, H. (2016). Analysis of local ice crystal growth in snow. *Journal of Glaciology*, *62*(232), 378–390. https://doi.org/10.1017/jog.2016.32

Lehning, M., Bartelt, P., Brown, B., & Fierz, C. (2002). A physical SNOWPACK model for the Swiss avalanche warning Part III: Meteorological forcing, thin layer formation and evaluation. *Cold Regions Science and Technology*, *16*(3), 169–184. https://doi.org/10.1016/S0165-232X(02)00072-1

Libbrecht, K. G. (2005). The physics of snow crystals. *Reports on Progress in Physics*, *68*(4), 855–895. https://doi.org/10.1088/0034-4885/68/4/R03

Libbrecht, K. G. (2019). Snow crystals. arXiv preprint arXiv:1910.06389. Retrieved from https://arxiv.org/abs/1910.06389

19422466, 2022, 9, Downloaded from https://agupubs.onlinelibrary.wiley.com/doi/10.1029/2022MS002998 by Cochrane France, Wiley Online Library on [21/11/2022]. See the Terms and Conditions (https://onlinelibrary.wiley.com/terms-and-conditions) on Wiley Online Library for rules of use; OA articles are governed by the applicable Creative Commons License

Libbrecht, K. G., & Rickerby, M. E. (2013). Measurements of surface attachment kinetics for faceted ice crystal growth. *Journal of Crystal Growth*, *377*, 1–8. https://doi.org/10.1016/j.jcrysgro.2013.04.037

Löwe, H., Riche, F., & Schneebeli, M. (2013). A general treatment of snow microstructure exemplified by an improved relation for thermal conductivity. *The Cryosphere*, *7*(5), 1473–1480. https://doi.org/10.5194/tc-7-1473-2013

Löwe, H., Spiegel, J., & Schneebeli, M. (2011). Interfacial and structural relaxations of snow under isothermal conditions. *Journal of Glaciology*, *57*(203), 499–510. https://doi.org/10.3189/002214311796905569

Miller, D., Adams, E., & Brown, R. (2003). A microstructural approach to predict dry snow metamorphism in generalized thermal conditions. *Cold Regions Science and Technology*, *37*(3), 213–226. https://doi.org/10.1016/j.coldregions.2003.07.001

Murphy, D. M., & Koop, T. (2005). Review of the vapour pressures of ice and supercooled water for atmospheric applications. *Quarterly Journal of the Royal Meteorological Society: A journal of the atmospheric sciences, applied meteorology and physical oceanography*, *131*(608), 1539–1565. https://doi.org/10.1256/qj.04.94

Ogawa, N., Flin, F., & Brzoska, J. B. (2006). Representation of two curvatures of surface and its application to snow physics. *Memoirs of the Hokkaido Institute of Technology*, *34*, 81.

Petrenko, V. F., & Whitworth, R. W. (1999). *Physics of ice*. Oxford University Press Inc.

Proksch, M., Rutter, N., Fierz, C., & Schneebeli, M. (2016). Intercomparison of snow density measurements: Bias, precision, and vertical resolution. *The Cryosphere*, *10*(1), 371–384. https://doi.org/10.5194/tc-10-371-2016

Schleef, S., Löwe, H., & Schneebeli, M. (2014). Influence of stress, temperature and crystal morphology on isothermal densification and specific surface area decrease of new snow. *The Cryosphere*, *8*(5), 1825–1838. https://doi.org/10.5194/tc-8-1825-2014

Sei, T., & Gonda, T. (1989). The growth mechanism and the habit change of ice crystals growing from the vapor phase. *Journal of Crystal Growth*, *94*(3), 697–707. https://doi.org/10.1016/0022-0248(89)90094-8

Srivastava, P., Mahajan, P., Satyawali, P., & Kumar, V. (2010). Observation of temperature gradient metamorphism in snow by X-ray computed microtomography: Measurement of microstructure parameters and simulation of linear elastic properties. *Annals of Glaciology*, *51*(54), 73–82. https://doi.org/10.3189/172756410791386571

Thoemen, H., Walther, T., & Wiegmann, A. (2008). 3D simulation of macroscopic heat and mass transfer properties from the microstructure of wood fibre networks. *Composites Science and Technology*, *68*(3), 608–616. https://doi.org/10.1016/j.compscitech.2007.10.014

Vetter, R., Sigg, S., Singer, H. M., Kadau, D., Herrmann, H. J., & Schneebeli, M. (2010). Simulating isothermal aging of snow. *EPL (Europhysics Letters)*, *89*(2), 26001. https://doi.org/10.1209/0295-5075/89/26001

Vionnet, V., Brun, E., Morin, S., Boone, A., Faroux, S., Le Moigne, P., et al. (2012). The detailed snowpack scheme Crocus and its implementation in SURFEX v7.2. *Geoscientific Model Development*, *5*(3), 773–791. https://doi.org/10.5194/gmd-5-773-2012

Yokoyama, E., & Kuroda, T. (1990). Pattern formation in growth of snow crystals occurring in the surface kinetic process and the diffusion process. *Physical Review A*, *41*(4), 2038–2049. https://doi.org/10.1103/PhysRevA.41.2038

19422466, 2022, 9, Downloaded from https://agupubs.onlinelibrary.wiley.com/doi/10.1029/2022MS002998 by Cochrane France, Wiley Online Library on [21/11/2022]. See the Terms and Conditions (https://onlinelibrary.wiley.com/terms-and-conditions) on Wiley Online Library for rules of use; OA articles are governed by the applicable Creative Commons License